論文 / 著書情報
Article / Book Information

Title	Impacts of O2/(O2tAr) Flow Ratio on the Properties of Li-Doped NiO Thin Films Fabricated by Pressure-Gradient Radiofrequency Magnetron Sputtering
Authors	Yosuke Abe, Takahito Nishimura, Akira Yamada
Citation	Physica Status Solidi A, vol. 222, Issue 7, 2400497
Pub. date	2024, 12
DOI	https://doi.org/10.1002/pssa.202400497
Creative Commons	Information is in the article.

physica status solidi a
www.pss-a.com

Impacts of $O_2/(O_2+Ar)$ Flow Ratio on the Properties of Li-Doped NiO Thin Films Fabricated by Pressure-Gradient Radiofrequency Magnetron Sputtering

Yosuke Abe, Takahito Nishimura, and Akira Yamada*

Herein, Li-doped NiO thin films are deposited on glass substrates using pressure-gradient radiofrequency magnetron sputtering, with Ar and O_2 as sputtering gases. Following film fabrication, their crystal structures, optical features, and electrical properties are investigated as functions of O_2 flow rate to the total flow rate ($O_2/(O_2+Ar)$) of 10 sccm. The deposited films are also annealed at 600 °C for 1 h in an oxygen atmosphere. Notably, the resistivity of the as-deposited films decreases significantly by three orders of magnitude from 106 to 0.0232 Ω cm when the sputtering gas is changed from pure Ar to pure O_2. However, the transmittance decreases with increasing oxygen flow rate. Investigations on the temperature dependence of conductivity reveal hole conduction in the range of ≈320–420 K owing to small polaron hopping.

1. Introduction

Transparent-conductive-oxide (TCO) thin films have gained prominence in various application fields such as solar cells,[1,2] light-emitting diodes,[3] and gas sensors.[4] The most widely recognized TCO thin films, such as In_2O_3[5,6] and ZnO,[7,8] are typically n-type semiconductors. While these n-type TCO materials have been extensively researched and adopted, p-type TCO has not been studied as much as n-type TCO. Nevertheless, NiO, a p-type TCO material, has attracted significant attention owing to its remarkable electrical and optical properties.

NiO features a rock-salt crystal structure and is classified as a wide-bandgap semiconductor with a bandgap ranging from 3.6 to 4.0 eV.[9] While stoichiometric NiO exhibits a high resistivity of 10^{13} Ω cm,[10] nonstoichiometric NiO thin films demonstrate p-type conductivity owing to the presence of native defects such as Ni vacancies and interstitial oxygen.[9,11] However, these defects can deteriorate transparency, necessitating the use of dopants such as Li, Cu, and Ag to maintain high acceptor density and transparency. Among these, Li was selected as the dopant in this study owing to its reported ability to exhibit the lowest resistivity while maintaining transparency.[12] Furthermore, NiO is applied in UV light-emitting diodes,[13] UV photodetectors,[14] and transparent solar cells,[2] taking advantage of its wide bandgap and low resistivity. In addition, NiO is also used as a hole transport layer in solar cells, with applications extending to perovskite solar cells[15] and Cu_2ZnSnS_4 solar cells.[16] Notably, improving the back contact characteristics of $Cu(In,Ga)Se_2$ solar cells is essential to further increase their efficiency. Remarkably, introducing a p-type semiconductor with excellent electrical properties as a hole transport layer is anticipated to be beneficial in this context.[17]

To date, NiO thin films have been fabricated using several methods, including sputtering,[18–20] sol–gel deposition,[21,22] and pulsed laser deposition.[23] In this study, film deposition was conducted using pressure-gradient radiofrequency magnetron sputtering (PGS: pressure gradient sputtering). Deposition using PGS has been applied to materials such as CN[24] and AlN,[25] but there are few reports of fabricating oxides like NiO. Here, Li-doped NiO (NiO:Li) thin films were deposited on glass substrates using the PGS method. Subsequently, the crystal structure, electrical properties, and optical features of these films were examined with O_2 flow rate to the total flow rate. Additionally, after NiO film deposition, annealing was conducted at 600 °C for 1 h in O_2 atmosphere, and its effects were examined.

2. Experimental Section

NiO:Li thin films were deposited on glass substrates (Corning Eagle XG) using the PGS method with NiO–Li_2CO_3 (Ni:Li = 95:5 at%) targets. **Figure 1** depicts the structure of the PGS system. In conventional sputtering, the supplied gas spreads throughout the chamber as depicted by the blue line in the figure, resulting in an approximately constant pressure between the substrate and target. Conversely, in PGS, the gas is supplied from the side of the cathode, and a lid with a hole, partially covering the target, confines the gas near the target, creating a pressure

Y. Abe, T. Nishimura, A. Yamada
Department of Electrical and Electronic Engineering
Tokyo Institute of Technology
2-12-1 Ookayama, Meguro-ku, Tokyo 152-8550, Japan
E-mail: abe.y.bc@m.titech.ac.jp

The ORCID identification number(s) for the author(s) of this article can be found under https://doi.org/10.1002/pssa.202400497.

DOI: 10.1002/pssa.202400497

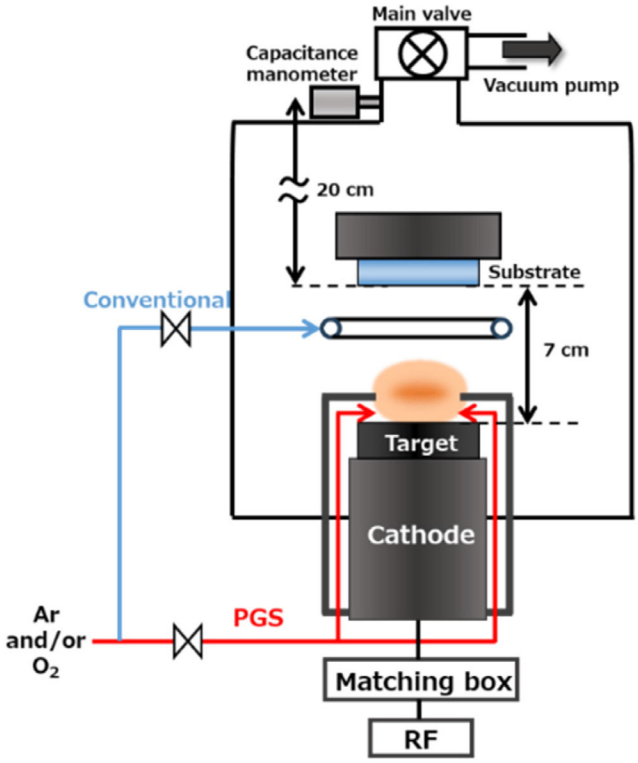

Figure 1. Schematic of the PGS system.

gradient between the substrate and target, as indicated by the red line. This configuration creates a high density of plasma above the target. Thus, the pressure near the substrate is maintained at a lower value relative to that near the target, resulting in a longer mean free path for sputtering particles and less plasma-induced damage to the substrate. In this study, local pressures near the target and substrate were measured using a pressure sensor (OKANO WORKS ATP-032S). This small, thermally conductive pressure sensor—with a length, width, and height of 35, 20, and 7 mm, respectively—was positioned close to the target and substrate to monitor local pressures before NiO:Li film deposition. Presputtering was performed for 20 min at a pressure of 0.25 Pa near the target in an Ar atmosphere. The substrate–target distance was maintained at 7 cm, and the background pressure was kept below 2×10^{-4} Pa. The RF power was set to 130 W (6.41 W cm^{-2}), and the substrates were not heated. The deposition time was fixed at 30 min. Sputtering was performed using Ar and O_2 gases, and their flow rates were controlled using a mass flow controller. The total pressure was maintained at 0.25 Pa near the target and 0.21 Pa near the substrate. The total flow rate of Ar and O_2 was fixed at 10 sccm and the ratio of O_2 flow rate to total flow rate ($O_2/(O_2 + Ar)$) was varied at 0, 10, 33, 66, and 100%. Hereafter, the ratio of the O_2 flow rate to the total flow rate will be referred to as the oxygen flow ratio. Following NiO:Li film deposition, annealing was performed at 600 °C for 1 h in an O_2 atmosphere with a pressure of 0.21 Pa near the substrates. The thicknesses of the NiO:Li films were estimated through spectroscopic ellipsometry using J. A. Woollam XLS-100. Additionally, the composition ratio of Ni and O was measured by X-ray fluorescence (XRF) analysis using SHIMADZU EDX-8000, on NiO:Li films deposited on p-type Si(100) wafers. Furthermore, the crystal structure was assessed using X-ray diffraction (XRD) equipment (Philips (PANalytical) X'Pert Pro MRD) equipped with Cu Kα radiation. The structures and compositions of the films were analyzed using scanning transmission electron microscopy (STEM) and energy-dispersive X-ray spectroscopy (EDS) (JEM-2100F) analyses. Meanwhile, optical properties were assessed through UV-vis spectroscopy using the SHIMADZU SolidSpec-3700 instrument. Furthermore, ionization energy measurements were conducted through photoelectron yield spectroscopy (PYS) analysis using BUNKOUKEIKI BIP-KV100. Finally, the electrical resistivity, Hall mobility, and carrier density were measured through the van der Pauw method for Hall effect measurements using the TOYO corporation ResiTest8400 apparatus.

3. Results and Discussion

3.1. Film Thickness and Compositional Analysis

Figure 2a illustrates the variation in deposition rate with oxygen flow ratio, as estimated by spectroscopic ellipsometry. Notably, the deposition rate decreases with increasing oxygen flow ratio,

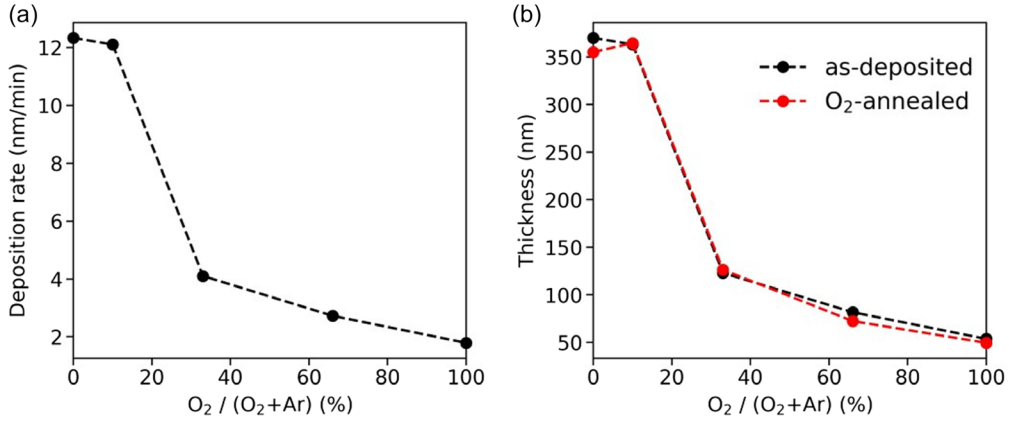

Figure 2. a) Variation in deposition rate with oxygen flow ratio, as estimated by spectroscopic ellipsometry. b) Film thicknesses measured 30 min after deposition and following O_2 annealing.

likely because oxygen has a lower sputtering rate compared to Ar.[26] Furthermore, it has been reported that an increase in oxygen gas reduces O_2^+ in the plasma and increases excited atomic oxygen (O*), promoting plasma neutralization, which in turn leads to a decrease in the deposition rate.[27]

Another factor contributing to this decrease is resputtering.[28,29] The particles that may collide with the substrate include positive ions, neutral particles, and negative ions. Among these, in the sputtering of oxides, the negative oxygen ions, which are accelerated by the self-bias and can possess energies of several hundred eV,[30] contribute the most to resputtering.[31] Figure S1 (Supporting Information) displays the target self-bias voltages measured during sputtering. Notably, a negative voltage of 500 V or higher is observed at all oxygen flow ratios. When O_2 is introduced as the sputtering gas, the negative ions of oxygen, generated by trapping electrons near the target, are accelerated to the substrate by the self-bias voltage, achieving energies of 500 eV. As a result, similar to the momentum exchange in typical sputtering caused by Ar^+ ion collisions with the target, these accelerated O^- ions sputter the deposited material on the substrate.[32]

As illustrated in Figure S2 (Supporting Information), the film surface sustains sputtering damage at an oxygen flow ratio of 33%. In our sputtering system, the substrate was placed on a holder grounded to the same potential as the chamber, with no bias applied. However, it is known that self-bias is similarly formed on the insulating substrate, though its magnitude is significantly smaller compared to the self-bias on the target.[33] Compared to results from conventional RF sputtering of other oxides, the deposition rate reduction observed in this study is larger,[26,27,34,35] suggesting that the PGS method may be more susceptible to the effects of self-bias. This is likely because the pressure near the substrate decreases in PGS, allowing O^- ions accelerated by the self-bias to collide with the substrate without significant attenuation by the sputtering gas. However, since substrate bias was not measured in this study, it is not feasible to quantify the extent of resputtering, making it difficult to conclude that resputtering is the primary cause of the observed changes in the deposition rate.

In this study, the low sputtering yield of oxygen,[26] plasma neutralization,[27] and resputtering were considered as the potential factors contributing to the reduction in deposition rate with oxygen flow ratio. However, based on the current experimental results, it is not straightforward to determine the dominant factor, leaving it as a topic for future research.

Figure 2b presents film thicknesses before and after O_2 annealing, depicting almost negligible changes between the two.

Figure 3 shows the composition ratio of O to Ni (O/Ni) measured by XRF. The relative values are shown with respect to the as-deposited film formed at 0% oxygen flow ratio. The O/Ni ratio increases with increasing oxygen flow ratio. As will be discussed later, the as-deposited film deposited at 0% oxygen flow ratio is already oxygen rich as shown in Table 2, indicating that all the films deposited in this study are oxygen rich and deviate from stoichiometry. Additionally, for films deposited at an oxygen flow ratio of 10% or higher, the O/Ni ratio decreases after O_2 annealing, whereas for the film deposited at 0% oxygen flow ratio, the O/Ni ratio increases. This suggests that when no oxygen is introduced during sputtering, oxygen is absorbed from the surface during the O_2-annealing process. On the other hand, when oxygen is introduced as a sputtering gas at 10% or higher, more oxygen desorbs from the surface than is absorbed.

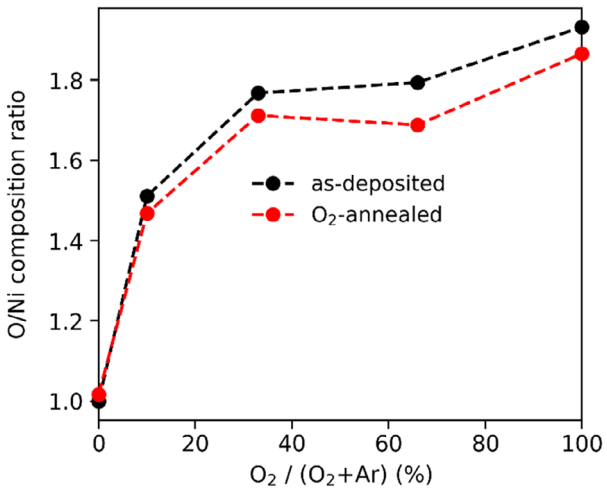

Figure 3. Variation of the O/Ni composition ratio with oxygen flow ratio. The relative values are shown with respect to the as-deposited film formed at 0% oxygen flow ratio.

3.2. Structural Characterization

Figure 4 displays the XRD results of the as-deposited films, while **Table 1** lists the parameters of crystal structure derived from the XRD analysis. Notably, the lattice constant (a) was computed using the following equations.

$$2dsin\theta = \lambda \tag{1}$$

$$\frac{1}{d^2} = \frac{h^2 + k^2 + l^2}{a^2} \tag{2}$$

In Equation (1), d denotes the lattice spacing, θ represents the Bragg angle, and λ indicates the X-ray wavelength (0.1542 nm).

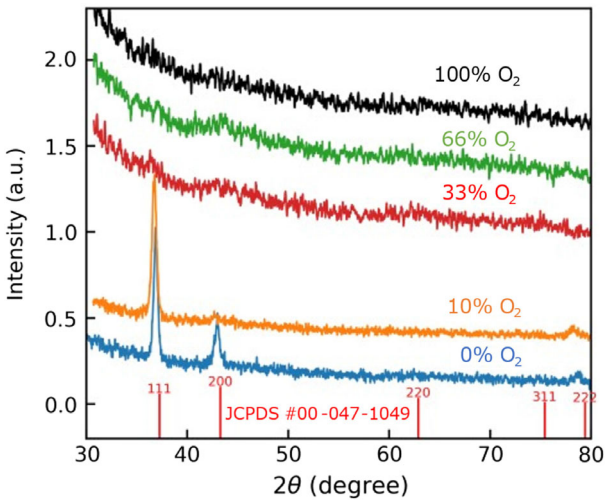

Figure 4. XRD patterns of the as-deposited NiO:Li thin films.

Table 1. 2θ, FWHM, lattice constant (a), and strain (ε) of NiO:Li thin films using the preferential orientation (111) observed at oxygen flow ratios of 0% and 10%.

Condition	$O_2/(O_2+Ar)$ [%]	2θ [°]	FWHM [°]	Lattice constant a [Å]	Strain ε [%]
As-deposited	0	36.97	0.467	4.211	0.818
	10	36.80	0.570	4.230	1.26
O_2 annealed	0	37.25	0.484	4.181	0.0915
	10	37.17	0.530	4.189	0.289

Meanwhile, in Equation (2), h, k, and l denote Miller indices. Notably, the strain (ε) is expressed as follows.[11]

$$\varepsilon = \frac{a - a_0}{a_0} \tag{3}$$

In Equation (3) and $a(0)$ has a value of 0.41771 nm (JCPDS #00-047-1049), corresponding to stoichiometric NiO.

As depicted in Figure 4, peaks corresponding to the (111), (200), and (222) planes are observed in the spectrum of the sample deposited under an oxygen flow ratio of 0%. In contrast, only peaks corresponding to the (111) and (222) planes are apparent in the spectrum of the sample deposited under an oxygen flow ratio of 10%. No peaks other than those attributed to NiO are observed at oxygen flow ratios of 0% and 10%, confirming the presence of a rock-salt crystal structure with a preferential (111) orientation. At oxygen flow ratios exceeding 33%, no peaks attributed to NiO are observed, indicating the formation of an amorphous phase.

The disappearance of the (200) peak in response to an increase in the oxygen flow ratio from 0 to 10% is attributed to the fact that the (111) plane is the densest oxygen plane. In addition to the oxygen from the target, oxygen from the sputtering gas is also supplied to the substrate, creating a more oxygen-aligned orientation. Table 1 details the full width at half maximum (FWHM), lattice constant (a), and strain (ε) values computed from the preferential orientation (111) observed at oxygen flow ratios of 0% and 10%. As indicated in Table 1, the FWHM increases with increasing the oxygen flow ratio, indicating a decrease in crystallinity. The lattice constant (a) of NiO:Li exceeds that of stoichiometric NiO owing to the larger ionic radius of Li^+ (0.76 Å) compared to that of Ni^{2+} (0.69 Å),[21] as well as the presence of interstitial oxygen. Furthermore, the lattice constant (a) and strain (ε) increase as the oxygen flow ratio increases from 0 to 10%, possibly owing to the increase in the amount of interstitial oxygen resulting from the increased oxygen concentration, as shown in Figure 3.

The XRD results of the O_2-annealed samples are depicted in Figure S3 (Supporting Information). After O_2 annealing, the peak corresponding to the (111) plane shifts to a higher angle at both oxygen flow ratios of 0% and 10%. Additionally, the lattice constant (a) and strain (ε) decrease, as indicated in Table 1, suggesting that the expansion owing to interstitial oxygen has relaxed by enhanced atomic diffusion resulting from thermal energy provision.

The STEM images displayed in Figure S4 (Supporting Information) indicate that the NiO:Li thin films feature columnar structures with triangular surface roughness profiles. **Figure 5** presents a magnified view of these images. Evidently, in the as-deposited film, voids are present at the grain boundaries between columnar grains, as indicated by the red arrows in Figure 5a. However, after O_2 annealing, these voids disappear, and the grains form a compact structure (Figure 5b). This change results from lateral grain growth owing to accelerated internal diffusion during annealing at 600 °C. **Table 2** lists the averaged values of the EDS elemental mappings displayed in Figure 5. Note that Li, being a light element, could not be detected by EDS. Despite being deposited at 0% oxygen flow ratio, the as-deposited films are rich in oxygen. This is because the mean free

Table 2. Averaged values of the EDS elemental mappings for NiO:Li films sputtered at 0% oxygen flow ratio depicted in the field of view shown in Figure 5.

Element	Atomic [%]	
	As-deposited	O_2 annealed
Si	0.1	0.1
C	1.1	1.8
O	59.1	59.7
Ni	39.6	38.3
O/Ni	1.49	1.56

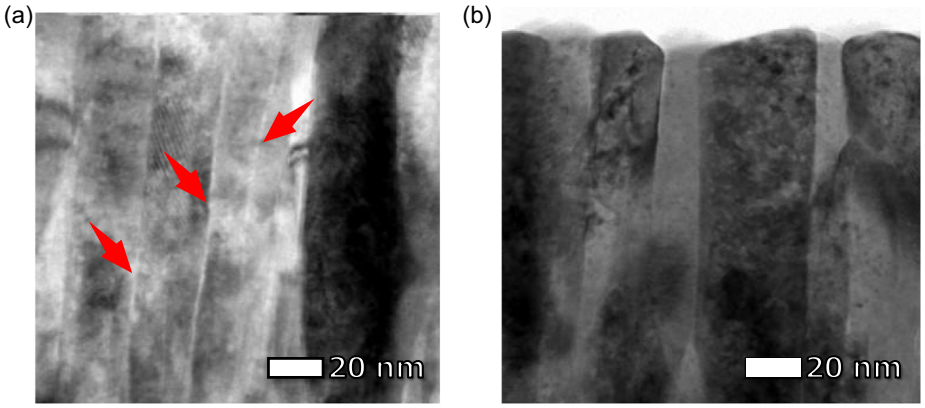

Figure 5. Cross-sectional STEM images of NiO:Li films sputtered at 0% oxygen flow ratio: a) as-deposited and b) O_2-annealed films.

path of oxygen at 0.21 Pa near the substrate is 48.2 cm, significantly longer than the substrate–target distance of 7 cm. Meanwhile, the corresponding mean free path of Ni is 5.00 cm, shorter than the substrate–target distance. Additionally, the oxygen content in the NiO:Li film sputtered at 0% oxygen flow ratio increases after O_2 annealing, consistent with the results in Figure 3, which resulted in decreased resistivity and transmittance, as detailed in the following sections.

3.3. Optical Analysis

Figure 6 displays the a) transmittance, b) average visible light (360–830 nm) transmittance, and c) bandgap versus oxygen flow ratio. Panel (b) indicates that, despite the decrease in film thickness under these conditions, the average transmittance drops significantly to below 5% when the oxygen flow ratio exceeds 33%, compared to when the oxygen flow ratio is below 10%. This result is attributed to the increase in the oxygen content within the film as shown in Figure 3. Their visible light transmittance decreases under oxygen-rich conditions owing to the formation of Ni vacancies, resulting in the creation of Ni^{3+} ions, known as color centers,[36] for charge conservation. Figure S5 (Supporting Information) displays the complex refractive index obtained through spectroscopic ellipsometry using the Tauc–Lorentz model[37] and the Drude model.[38] At oxygen flow ratios of 0% and 10%, where the XRD results confirmed crystallization, the refractive index (n) in the visible wavelength range is ≈2.4, consistent with previously reported values.[39,40] Furthermore, for oxygen flow ratios of 33% and above, the value of the extinction coefficient (k) exceeds those at oxygen flow ratios below 10%. This increase could be attributed to free carrier absorption caused by a high carrier density and the influence of Ni^{3+} color centers. In particular, at oxygen flow ratios of 66% and above, the increase in the value of the extinction coefficient (k) from the visible to near-infrared ranges explains the increased reflectance caused by plasma reflection, as illustrated in Figure S6 (Supporting Information).

As illustrated in Figure 6b, the average visible light transmittance improves after O_2-annealing for samples sputtered at oxygen flow ratios exceeding 10%. This improvement is attributed to the reduction in the quantities of native defects, such as interstitial oxygen and Ni vacancies, which form Ni^{3+} color centers.[9,41] In contrast, the average visible light transmittance of the sample sputtered at 0% oxygen flow ratio decreases owing to an increase in the oxygen content of the film, as indicated in Figure 3 and Table 2.

Next, bandgap calculations were performed using the Tauc plot, as depicted in Figure S7 (Supporting Information). For the as-deposited films formed at oxygen flow ratios of 0% and 10%, a sharp increase in absorption occurs near the absorption edge. However, for films deposited at oxygen flow ratios exceeding 33%, absorption begins gradually at energies lower than the absorption edge, indicating the occurrence of parasitic absorption owing to substantial amounts of native defects in the bandgap and the extension of free carrier absorption close to the band edge. The bandgap of NiO:Li films formed at an oxygen flow ratio of 0% is ≈3.5 eV, which is lower than that of NiO (3.6–4.0 eV).[9] Notably, this reduction is attributed to decreased crystallinity resulting from Li doping, which elongates the band tail and reduces the bandgap.[42] After O_2-annealing, the bandgap widens at all oxygen flow ratios, likely owing to the reduction of the band tail.

Figure 7a depicts ionization energies calculated from PYS spectrum shown in Figure S8 (Supporting Information). Notably, during PYS measurements, sample surfaces are irradiated with UV radiation to generate photoelectrons. In semiconductors, by plotting the photoelectron yield$^{1/3}$ against photon energy, the ionization energy can be determined from the threshold, and the valence band maximum (VBM) can be estimated.[43,44] Previous studies have reported ionization energies of NiO ranging 5.04–5.7 eV.[42,45,46] Note that these values can vary depending on factors such as the composition ratio of NiO, crystallinity, and surface conditions. Other reports suggest an increase in ionization energy with increasing oxygen concentration in the film.[42]

As depicted in Figure 7a, the ionization energies of films formed at oxygen flow ratios above 10% tend to exceed that observed at an oxygen flow ratio of 0%, likely attributed to the increase in the oxygen content of the film. After O_2 annealing, the ionization energy of the film formed at an oxygen flow ratio of 0% increases, whereas those for the films formed at oxygen flow ratios above 10% decrease. From Figure 3, it is observed that only the film with 0% oxygen flow ratio shows an increase in oxygen content after O_2 annealing. Therefore, it is anticipated that the observed trend in ionization energy changes due to O_2 annealing is attributed to the variation in oxygen content within the film. On the other hand, changes in ionization energy cannot be fully explained by oxygen concentration alone, necessitating further measurements of surface states and electronic states.

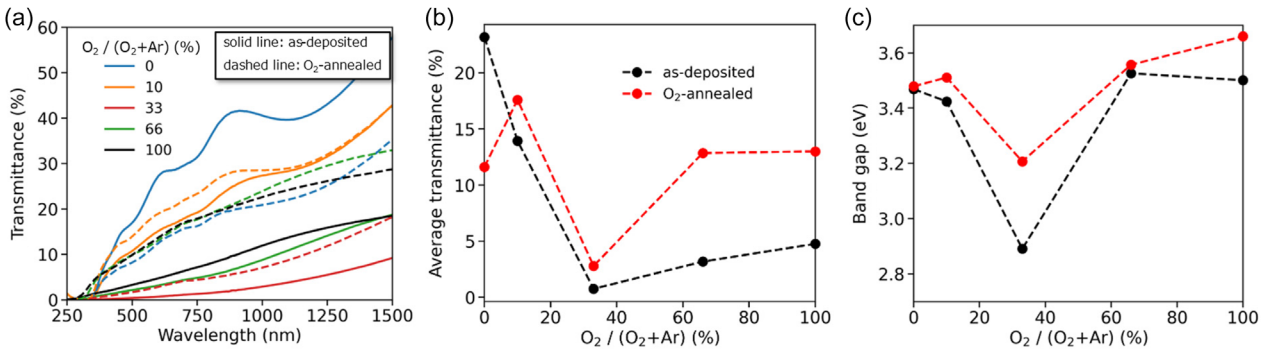

Figure 6. Variation in the a) transmittance, b) average visible light (360–830 nm) transmittance, and c) bandgap of the films with oxygen flow ratio.

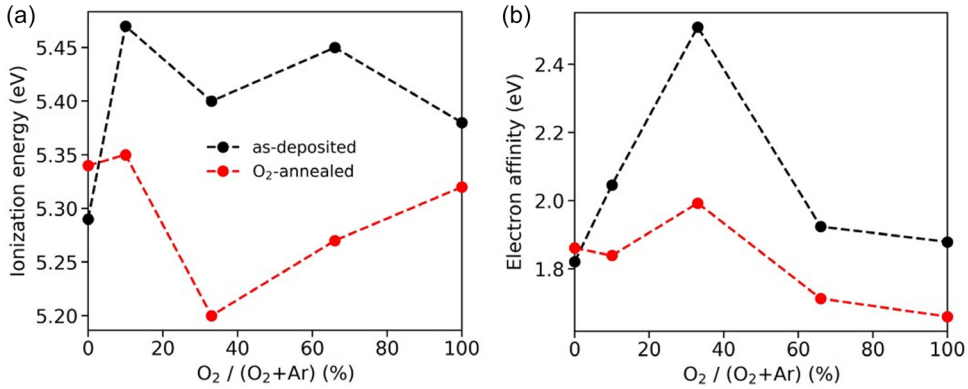

Figure 7. a) Variation in the ionization energy and b) the electron affinity with oxygen flow ratio. The ionization energy was calculated by plotting the photoelectron yield$^{1/3}$ against photon energy as shown in Figure S8 (Supporting Information). The electron affinity is estimated using the following relation: electron affinity = ionization energy (VBM) − bandgap.

Figure 7b presents the electron affinity, estimated from the ionization energy and bandgap (electron affinity = ionization energy − bandgap). Notably, apart from the as-deposited film formed at an oxygen flow ratio of 33%, the electron affinities of all other films range from 1.66 to 2.05 eV, closely matching the reported values of 1.33–1.85 eV.[47–50] The as-deposited film formed at an oxygen flow ratio of 33% exhibits a large electron affinity of 2.51 eV, likely owing to a low estimated bandgap, resulting from a large amount of parasitic absorption in the visible light range, as shown in Figure S7a (Supporting Information).

3.4. Electrical Properties

To examine the electrical properties of the films, their resistivities were measured using the van der Paw method, while their carrier density and mobility values were evaluated through Hall measurements. **Figure 8**a displays the obtained resistivity values. Notably, the resistivity of the as-deposited films decreases by three orders of magnitude, from 106 to 0.0232 Ω cm, as the sputtering gas is switched from pure Ar to pure O_2. This significant decrease is attributed to the suppression of oxygen vacancies, which act as donor defects, and an increase in the quantities of interstitial oxygen and numbers of Ni vacancies, acting as acceptor defects,[9,11,51] thereby increasing the net acceptor density. Following O_2 annealing, only the film formed at an oxygen flow ratio of 0% presents a decreased resistivity, likely attributed to an increase in the number of Ni vacancies caused by surface oxygen absorption. Conversely, the resistivity values of films formed at oxygen flow ratios exceeding 10% increase after O_2 annealing. Concurrently, the dependence of resistivity on the oxygen flow ratio weakens. This increase is likely attributed to the reduction in the number of native defects, such as Ni vacancies and interstitial oxygen, owing to enhanced internal diffusion during O_2 annealing and the decrease in oxygen content shown in Figure 3. This observation is consistent with the increased transmittance depicted in Figure 6a,b.

Figure 8b presents the hall measurement results for the O_2-annealed films. Notably, NiO:Li thin films have been demonstrated to exhibit p-type conductivity at oxygen flow ratios of up to 66% after O_2 annealing. Under other conditions, the carrier type is unstable and easily varies with repeated measurements, complicating the determination of p-type conductivity. The lower limit for mobility measurement using the Hall method is 1×10^{-3} $cm^2\,V^{-1}\,s^{-1}$, and the Hall mobility likely falls below this measurement limit. Thus, the carrier types of O_2-annealed samples

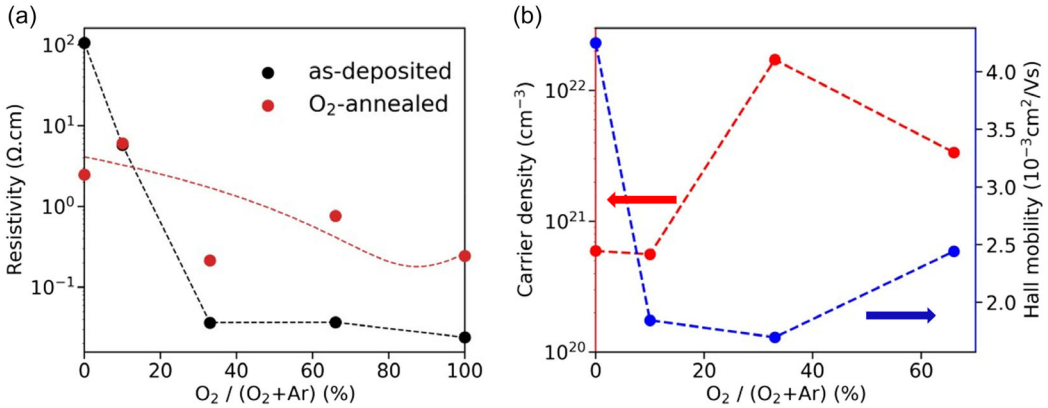

Figure 8. a) Resistivities of the films measured using the van der Pauw method and b) their Hall measurement results after O_2 annealing.

deposited at oxygen flow ratios of up to 66% can be determined reliably. As depicted in Figure 8b, the carrier density increases to $10^{22}\,cm^{-3}$ at an oxygen flow ratio of 33%, attributed to the high densities of interstitial oxygen and Ni vacancies. Mobility values, on the order of 10^{-3} $cm^2\,V^{-1}\,s^{-1}$ for all samples, significantly decrease from 4.25×10^{-3} to $1.84 \times 10^{-3}\,cm^2\,V^{-1}\,s^{-1}$ as the oxygen flow ratio increases from 0 to 10%.

NiO:Li films produced in this study tend to exhibit a higher acceptor density compared to those made using conventional RF sputtering with targets containing similar or higher levels of Li.[12,41,51] This may be due to the lower pressure near the substrate in PGS which causes sputtered particles and O^- accelerated by self-bias to collide with the substrate with high energy, potentially generating a greater number of interstitial oxygen. Verification of this hypothesis requires a comparison of the interstitial oxygen content between films produced by conventional RF sputtering and PGS using techniques such as XPS.[52,53]

On the other hand, the resistivity of NiO:Li recently reported in the literature is ≈0.18 and 0.3 Ω cm[54,55] for spin-coating methods, 2.3×10^2 Ω cm for ultrasonic pyrolysis spray method,[56] 9.9 Ω cm for mist chemical vapor deposition,[57] and 0.089 Ω cm for pulsed laser deposition.[45] Comparing these values with the NiO:Li thin films identified as p-type in this study, the values obtained here are not particularly outstanding. Therefore, it cannot be concluded that the PGS method enables the fabrication of high-quality, low-resistivity films.

To analyze the mechanism of hole conduction, we analyzed the temperature dependence of conductivity. The primary conduction mechanisms for NiO include band and hopping conduction.[45,58–60] Notably, the top of the valence band of NiO comprises the 3d orbitals of Ni,[58] and the holes produced in NiO move through these highly localized 3d orbitals. Consequently, these holes migrate from one site to another via hopping, driven by thermal activation. This process is known as small polaron hopping (SPH), and the corresponding conductivity can be expressed as follows.[45,60,61]

$$\sigma = \frac{\sigma_0}{T} exp\left(-\frac{E_a}{kT}\right) \tag{4}$$

In Equation (4), E_a denotes the activation energy for SPH, k represents Boltzmann's constant, and T indicates the absolute temperature. **Figure 9** illustrates the temperature dependence of the conductivity. Notably, the conductivity values of both the as-deposited and O_2-annealed films increase with increasing temperature. **Figure 10** presents the fitting results derived from the SPH model. Notably, the conductivity values of the

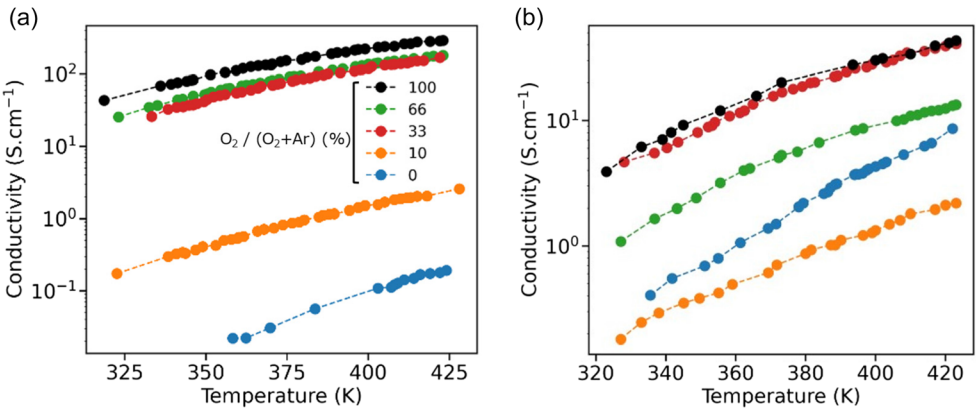

Figure 9. Temperature dependence of the conductivity values of the a) as-deposited and b) O_2-annealed films in the range of ≈320–420 K.

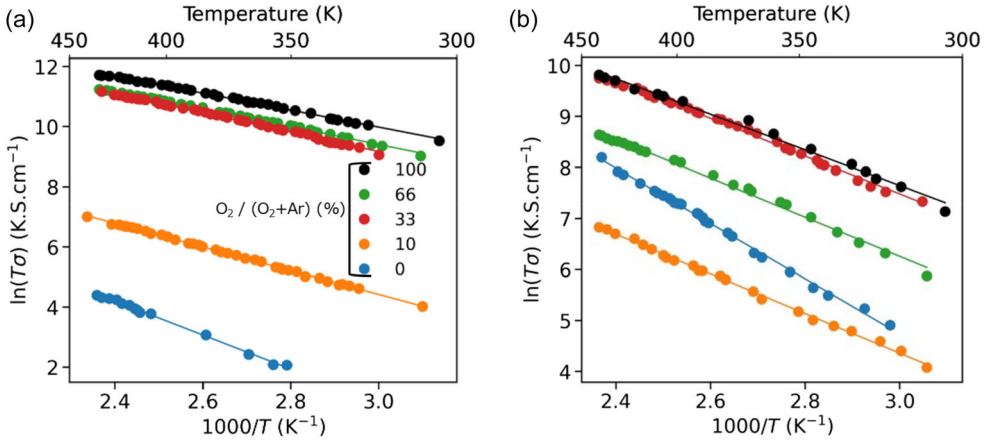

Figure 10. Fitting results of the temperature dependence of the conductivity (Figure 9) for a) as-deposited and b) O_2-annealed films using Equation (4).

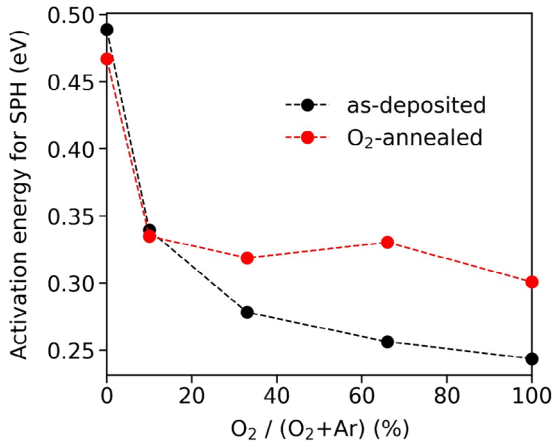

Figure 11. Activation energy (E_a) for SPH calculated from the fitting results of Figure 10 based on Equation (4).

as-deposited and O_2-annealed films formed under varying oxygen flow ratios are well fitted by the SPH model. When holes conduct in the 2p orbitals due to band conduction, the carrier concentration becomes independent of the temperature owing to degeneracy at high carrier densities exceeding 10^{20} cm^{-3}. Similarly, scattering due to ionized impurities also becomes independent of temperature.[62] Additionally, the increase in conductivity with temperature may be influenced by grain boundary scattering; however, in NiO, Ni vacancies at grain boundaries are more numerous than those in the bulk,[60,63] implying the absence of barriers at grain boundaries, unlike n-type TCOs.[62] Thus, the increase in conductivity with temperature shown in Figure 9 is likely attributed to the activation of hopping conduction driven by thermal energy, which accounts for the low mobility values on the order of 10^{-3} cm^2 V^{-1} s^{-1}.

Figure 11 depicts the calculated activation energies for SPH. Notably, the activation energy of the film formed at an oxygen flow ratio of 0% is ≈0.48 eV, which corresponds to the binding energy of a hole at the Li site.[58] Overall, the activation energy tends to decrease with increasing the oxygen flow ratio, indicating a shift in the dominant acceptor origin to a shallower acceptor.[64] The O_2-annealing increase observed in the activation energies of samples formed at oxygen flow ratios above 33% is likely attributed to reduced lattice disorder resulting in suppressed band broadening and weaker overlap between individual Ni sites.[65]

4. Conclusion

In summary, NiO:Li thin films were prepared using PGS, following which their crystallinity, optical properties, and electrical properties were investigated as functions of the oxygen flow ratio. Additionally, after NiO:Li film deposition, annealing was conducted at 600 °C for 1 h in O_2 atmosphere, and its effects were examined.

Notably, the deposition rate decreased with increasing the oxygen flow ratio, and sputtering in pure oxygen resulted in ≈6-fold reduction compared to pure Ar. The composition ratio of O to Ni increased with increasing the oxygen flow ratio. XRD results revealed NiO:Li thin films formed at oxygen flow ratios below 10% had a rock-salt crystal structure with a preferential (111) orientation. At oxygen flow ratios exceeding 33%, no peaks attributed to NiO were observed, indicating the formation of an amorphous phase. The average transmittance dropped significantly when the oxygen flow ratio exceeded 33%, compared to when the oxygen flow ratio was below 10%. In the as-deposited state, the resistivity of the films decreased from 106 to 0.0232 Ω cm when switching the sputtering gas from pure Ar to pure O_2. Following O_2 annealing, only the film formed at an oxygen flow ratio of 0% presented a decreased resistivity owing to the increase in oxygen content. Conversely, the resistivity values of films formed at oxygen flow ratios exceeding 10% increased after O_2 annealing. NiO:Li films formed in this study using PGS tended to have a higher acceptor density than those made using conventional RF sputtering. This may be due to the lower pressure near the substrate in PGS which causes sputtered particles and O^- accelerated by self-bias to collide with the substrate with high energy, potentially generating a greater number of interstitial oxygen atoms. The temperature dependence of conductivity revealed the mechanism of hole conduction in the range of ≈320–420 K based on the SPH model.

Acknowledgements

This research was supported by the New Energy and Industrial Technology Development Organization (NEDO), and the authors would like to thank all parties involved. A part of this research was also supported by JSPS Grant-in-Aid for Scientific Research B (22H01531).

Conflict of Interest

The authors declare no conflict of interest.

Data Availability Statement

The data that support the findings of this study are available from the corresponding author upon reasonable request.

Keywords

hole transport layers, pressure gradient sputtering, p-type transparent conductive oxides, sputtering, transparent conductive oxides

Received: June 11, 2024
Revised: November 23, 2024
Published online: December 8, 2024

[1] E. A. Gibson, A. L. Smeigh, L. Le Pleux, J. Fortage, G. Boschloo, E. Blart, Y. Pellegrin, F. Odobel, A. Hagfeldt, L. Hammarström, *Angew. Chem.* **2009**, *121*, 4466.
[2] M. Patel, H. S. Kim, J. Kim, J. H. Yun, S. J. Kim, E. H. Choi, H. H. Park, *Sol. Energy Mater. Sol. Cells* **2017**, *170*, 246.
[3] Y. Y. Xi, Y. F. Hsu, A. B. Djurišić, A. M. C. Ng, W. K. Chan, H. L. Tam, K. W. Cheah, *Appl. Phys. Lett.* **2008**, *92*, 113505.
[4] J. A. Dirksen, K. Duval, T. A. Ring, *Sens. Actuators, B* **2001**, *80*, 106.
[5] T. Koida, H. Fujiwara, M. Kondo, *Sol. Energy Mater. Sol. Cells* **2009**, *93*, 851.

[6] T. Koida, J. Nishinaga, Y. Ueno, H. Higuchi, H. Takahashi, M. Iioka, Y. Kamikawa, H. Shibata, S. Niki, *Prog. Photovolt.* **2019**, *27*, 491.
[7] W. W. Wenas, A. Yamada, K. Takahashi, M. Yoshino, M. Konagai, *J. Appl. Phys.* **1991**, *70*, 7119.
[8] S. Cornelius, M. Vinnichenko, N. Shevchenko, A. Rogozin, A. Kolitsch, W. Möller, *Appl. Phys. Lett.* **2009**, *94*, 042103.
[9] H. Sato, T. Minami, S. Takata, T. Yamada, *Thin Solid Films* **1993**, *236*, 27.
[10] M. Nachman, L. N. Cojocaru, L. V. Rîbco, *Phys. Status Solidi B* **1965**, *8*, 773.
[11] J. D. Hwang, T. H. Ho, *Mater. Sci. Semicond. Process.* **2017**, *71*, 396.
[12] K. O. Egbo, C. E. Ekuma, C. P. Liu, K. M. Yu, *Phys. Rev. Mater.* **2020**, *4*, 104603.
[13] C. Song, G. Xiang, J. Zhang, Z. Yue, X. Zhang, B. Ding, Y. Jin, P. Wang, H. Li, H. He, L. Wang, Y. Zhao, H. Wang, *Opt. Mater.* **2023**, *145*, 114452.
[14] M. Jia, F. Wang, L. Tang, J. Xiang, K. S. Teng, S. P. Lau, Y. Lü, *Opt. Laser Technol.* **2023**, *157*, 108634.
[15] Z. Lv, G. Liu, Z. Wang, Y. Gao, W. Lu, J. Wei, L. Zhang, P. Wang, Y. Yan, Y. Shi, J. Bian, *ACS Appl. Mater. Interfaces* **2024**, *16*, 54272.
[16] A. Ait Abdelkadir, E. Oublal, M. Sahal, A. Gibaud, *Results Opt.* **2022**, *8*, 100257.
[17] Y. Abe, R. Fukuda, T. Nishimura, A. Yamada, presented at *PVSEC-34. Systematic Analysis of Ag Addition Effects on Bulk and Interface Properties in CIGSe Solar Cells*, China, November, **2023**.
[18] I. Hotový, D. Búc, Š. Haščík, O. Nennewitz, *Vacuum* **1998**, *50*, 41.
[19] T. F. Chen, A. J. Wang, B. Y. Shang, Z. L. Wu, Y. L. Li, Y. S. Wang, *J. Alloys Compd.* **2015**, *643*, 167.
[20] M. Guziewicz, J. Grochowski, M. Borysiewicz, E. Kaminska, J. Z. Domagala, W. Rzodkiewicz, B. S. Witkowski, K. Golaszewska, R. Kruszka, M. Ekielski, A. Piotrowska, *Opt. Appl.* **2011**, *41*, 431.
[21] W. Guo, K. N. Hui, K. S. Hui, *Mater. Lett.* **2013**, *92*, 291.
[22] F. S. Hashim, K. H. Mohsin, *J. Kufa Phys.* **2015**, *7*, 43.
[23] D. Franta, B. Negulescu, L. Thomas, P. R. Dahoo, M. Guyot, I. Ohlídal, J. Mistrík, T. Yamaguchi, *Appl. Surf. Sci.* **2005**, *244*, 426.
[24] M. Aono, M. Terauchi, Y. K. Sato, K. Morita, T. Inoue, K. Kanda, K. Yonezawa, *Appl. Surf. Sci.* **2023**, *635*, 157677.
[25] Y. Terai, K. Haraguchi, R. Ichinose, H. Oota, K. Yonezawa, *J. Appl. Phys.* **2023**, *62*, SA1003.
[26] H. W. Ryu, G. P. Choi, W. S. Lee, J. S. Park, *J. Mater. Sci.* **2004**, *39*, 4375.
[27] C. Li, D. Wang, Z. Li, X. Li, T. Kawaharamura, M. Furuta, *J. Mater.* **2013**, *2013*, 547271.
[28] Z. Xie, Z. Li, H. Lu, Y. Wang, M. Wu, S. Yang, Y. Liu, *J. Mater. Sci. Mater. Electron.* **2020**, *31*, 19056.
[29] L. W. Rieth, P. H. Holloway, *J. Vac. Sci. Technol. A* **2004**, *22*, 20.
[30] A. Bikowski, T. Welzel, K. Ellmer, *Appl. Phys. Lett.* **2013**, *102*, 242106.
[31] Y. Cai, W. Liu, Q. He, Y. Zhang, T. Yu, Y. Sun, *Appl. Surf. Sci.* **2010**, *256*, 1694.
[32] D. J. Kester, R. Messier, *J. Mater. Res.* **1993**, *8*, 1928.
[33] H. R. Koenig, I. Maissel, *IBM J. Res. Dev.* **1970**, *14*, 168.
[34] S. Ben Amor, B. Rogier, G. Baud, M. Jacquet, M. Nardin, *Mater. Sci. Eng. B* **1998**, *57*, 28.
[35] B. Abdallah, A. K. Jazmati, R. Refaai, *Mat. Res.* **2017**, *20*, 607.
[36] H. H. Txppns, *Phys. Rev. B* **1970**, *1*, 126.
[37] G. E. Jellison, F. A. Modine, *Appl. Phys. Lett.* **1996**, *69*, 371.
[38] J. Steinhauser, S. Faÿ, N. Oliveira, E. Vallat-Sauvain, C. Ballif, *Appl. Phys. Lett.* **2007**, *90*, 142107.
[39] H. L. Lu, G. Scarel, M. Alia, M. Fanciulli, S. J. Ding, D. W. Zhang, *Appl. Phys. Lett.* **2008**, *92*, 222907.
[40] A. Venter, J. R. Botha, *S. Afr. J. Sci.* **2011**, *107*, 1.
[41] X. Chu, J. Leng, J. Liu, Z. Shi, W. Li, S. Zhuang, H. Yang, G. Du, J. Yin, *J. Mater. Sci. Mater. Electron.* **2016**, *27*, 6408.
[42] Z. Qiu, H. Gong, G. Zheng, S. Yuan, H. Zhang, X. Zhu, H. Zhou, B. Cao, *J. Mater. Chem. C* **2017**, *5*, 7084.
[43] M. Sugiyama, T. Shimizu, D. Kawade, K. Ramya, K. T. Ramakrishna Reddy, *J. Appl. Phys.* **2014**, *115*, 083508.
[44] Y. Nakayama, S. MacHida, D. Tsunami, Y. Kimura, M. Niwano, Y. Noguchi, H. Ishii, *Appl. Phys. Lett.* **2008**, *92*, 153306.
[45] J. Y. Zhang, W. W. Li, R. L. Z. Hoye, J. L. MacManus-Driscoll, M. Budde, O. Bierwagen, L. Wang, Y. Du, M. J. Wahila, L. F. J. Piper, T. L. Lee, H. J. Edwards, V. R. Dhanak, K. H. L. Zhang, *J. Mater. Chem. C* **2018**, *6*, 2275.
[46] E. L. Ratcliff, J. Meyer, K. X. Steirer, A. Garcia, J. J. Berry, D. S. Ginley, D. C. Olson, A. Kahn, N. R. Armstrong, *Chem. Mater.* **2011**, *23*, 4988.
[47] H. Wu, L. S. Wang, *J. Chem. Phys.* **1997**, *107*, 16.
[48] D. Kawade, S. F. Chichibu, M. Sugiyama, *J. Appl. Phys.* **2014**, *116*, 163108.
[49] M. D. Irwin, J. D. Servaites, D. B. Buchholz, B. J. Leever, J. Liu, J. D. Emery, M. Zhang, J. H. Song, M. F. Durstock, A. J. Freeman, M. J. Bedzyk, M. C. Hersam, R. P. H. Chang, M. A. Ratner, T. J. Marks, *Chem. Mater.* **2011**, *23*, 2218.
[50] M. Patel, H. S. Kim, J. Kim, *Adv. Electron. Mater.* **2015**, *1*, 1500232.
[51] M. Sugiyama, H. Nakai, G. Sugimoto, A. Yamada, S. F. Chichibu, *Jpn. J. Appl. Phys.* **2016**, *55*, 088003.
[52] L. Wang, J. Liu, L. Zhao, X. Fan, Q. Wang, *Opt. Mater.* **2021**, *122*, 111672.
[53] J. D. Hwang, H. Y. Chen, Y. H. Chen, T. H. Ho, *Nanotechnology* **2018**, *29*, 295705.
[54] J. Arunodaya, T. Sahoo, *Mater. Res. Express* **2019**, *7*, 016405.
[55] Y. Kokubun, S. Nakagomi, *Phys. Status Solidi B* **2020**, *257*, 2000330.
[56] V. H. López-Lugo, M. García-Hipólito, A. Rodríguez-Gómez, J. C. Alonso-Huitrón, *Nanomaterials* **2023**, *13*, 13010197.
[57] M.-S. Kong, M.-S. Park, S.-Y. Bae, *J. Mater. Sci. Eng.* **2024**, *310*, 117736.
[58] D. Adler, J. Feinleib, *Phys. Rev. B* **1970**, *2*, 3112.
[59] T. Dutta, P. Gupta, A. Gupta, J. Narayan, *J. Appl. Phys.* **2010**, *108*, 083715.
[60] S. A. Makhlouf, M. A. Kassem, M. A. Abdel-Rahim, *J. Mater. Sci.* **2009**, *44*, 3438.
[61] E. Antolini, *Mater. Chem. Phys.* **2003**, *82*, 937.
[62] D. H. Zhang, H. L. Ma, *Appl. Phys. A* **1996**, *62*, 487.
[63] A. Atkinson, R. I. Taylor, *Philos. Mag. A* **1981**, *43*, 979.
[64] J. G. Amen, A. G. Jordan, *J. Phys. Chem. Solids* **1968**, *29*, 2153.
[65] R. Karsthof, M. Grundmann, M. A. Anton, F. Kremer, *Phys. Rev. B* **2019**, *99*, 235201.